Characterizing and Improving the Thermal Stability of Organic Photovoltaics Based on Halogen-rich Non-fullerene Acceptors

Kan Ding[1], Yongxi Li[2], Stephen R. Forrest *[1,2,3]

[1]*Department of Physics, University of Michigan*

[2] *Department of Electrical Engineering and Computer Science, University of Michigan*

[3]*Departments of Material Science and Engineering, University of Michigan*

Ann Arbor, MI 48109, USA

ABSTRACT

The thermal stability of inverted, halogen-rich non-fullerene acceptor (NFA)-based organic photovoltaics (OPVs) with MoO_x as the hole transporting layer is studied at temperatures up to 80°C. Over time, the power conversion efficiency shows a "check-mark" shaped thermal aging pattern, featuring an early decrease, followed by a long-term recovery. A high Cl concentration at the BHJ/MoO_x interface in the thermally aged device is found using energy dispersive X-ray spectroscopy. X-Ray photoelectron spectroscopy shows that the MoO_x is chlorinated after thermal aging. With bulk quantum efficiency analysis, we propose an explanation to the check-mark shaped pattern. Inserting a thin C_{70} layer between the BHJ and MoO_x suppresses the thermal degradation mechanisms, resulting in 3 orders of magnitude increase in device lifetime at 80°C.

*Corresponding author, email stevefor@umich.edu

1. Introduction

Non-fullerene acceptor (NFA)-based organic photovoltaics (OPVs) have drawn attention due to their high power conversion efficiencies (PCEs).[1-4] However, NFA-based OPVs often have poor thermal stabilities, significantly limiting their outdoor applications.[5-10] Previous work has shown that OPV thermal degradation can be related to time-dependent changes to the bulk heterojunction (BHJ),[11-13] the BHJ/hole transporting layer (HTL) interface,[14-19] BHJ/electron transporting layer (ETL) interface,[20] or the electrodes.[21-24] Among various sources of these changes, MoO_x layer is found to be highly correlated to the OPV thermal degradation when used as an HTL.[14-16, 19, 25] However, a complete understanding of the mechanisms behind the MoO_x-induced thermal degradation is still lacking.

Previously, we demonstrated high intrinsic photostability for an inverted NFA-based OPV structure with MoO_x and ZnO as the HTL and ETL, respectively, both protected by ultrathin interfacial layers.[26] A thin C_{70} interfacial layer placed between the BHJ and MoO_x was found to considerably improve the operational lifetime. Likewise, a self-assembled monolayer at the ZnO/HTL had a similar significant effect on extending the device lifetime. In this work, we specifically focus on the role played by C_{70} in regarding OPV thermal degradation mechanism. In the absence of the C_{70} buffer, the PCE exhibits a "check-mark" shaped aging pattern exhibiting a rapid initial decrease followed by a slower recovery. Energy dispersive X-ray spectroscopy (EDS) shows a high Cl concentration at the BHJ/MoO_x interface, and X-ray photoelectron spectroscopy (XPS) shows the MoO_x is chlorinated after the thermal aging process. Using bulk quantum efficiency (BQE) analysis, we identify two thermal degradation modes. The first results in a decrease and recovery of the BQE. The second mode results in an increasing interfacial voltage loss that affects the layers peripheral to the BHJ (i.e. the electrodes, HTL, and BHJ/HTL interfaces).

Based on these results, we propose mechanisms responsible for the thermally-induced degradation observed.

Furthermore, we show that inserting a thin C_{70} layer between the BHJ and MoO_x almost eliminates the first mode, while largely suppressing the second, hence significantly enhancing the OPV thermal stability.[27] Specifically, the device lifetime (its T_{80}, or the time it take the cell to lose 20% of its initial efficiency) at 80°C improves from 20 min to 800 h when aged in the dark.

2. Results

We study a semi-transparent BHJ comprising a blend of the archetype donor, poly[4,8-bis(5-(2-ethylhexyl)thiophen-2-yl)benzo[1,2-b;4,5-b']dithiophene-2,6-diyl-alt-(4-(2-ethylhexyl)-3-fluorothieno[3,4-b]thiophene-)-2-carboxylate-2-6-diyl]] (PCE-10), and the Cl-rich acceptor, 4,4,10,10-tetrakis(4-hexylphenyl)-5,11-(2-ethylhexyloxy)-4,10-dihydrodithienyl[1,2b:4,5b'] benzodithiophene -2,8-diyl)bis(2-(3-oxo-2,3-dihydroinden-5,6-dichloro-1-ylidene)malononitrile) (BT-CIC). This material system is a promising candidate for semi-transparent window applications, and has demonstrated exceptionally high photostability.[26, 28-30] The OPV structure lacking a C_{70} anode buffer (the control) shown in the inset of Fig. 1(a) is: ITO (thickness: 150nm)/ZnO (30 nm)/4-((1,3-dioxo-1,3-dihydro-2H-inden-2-ylidene)methyl)benzoic acid (IC-SAM)/PCE-10:BT-CIC, 1:1.5, 80 nm/MoO_x (10 nm)/Ag (100 nm).

Figure 1(a) shows the time evolution of the current density- voltage (*J-V*) characteristics of the "control" OPV at 50°C. After 600 h, the short-circuit current (J_{sc}) decreased from 23.4 ± 0.3 mA/cm^2 to 18.0 ± 0.3 mA/cm^2, the open-circuit voltage (V_{oc}) from 0.69 ± 0.01 V to 0.64 ± 0.01 V, the fill factor (FF) from 0.69 ± 0.01 to 0.58 ± 0.01, and PCE from 11.3 ± 0.2 % to 6.6 ± 0.2 %.

Figure 1(b) shows the time evolution of the *J-V* characteristics when a 2-nm-thick C_{70} layer is inserted between the BHJ and the MoO_x (the "buffered" device).[31] The degradation rate is significantly suppressed, with only a small decrease in PCE of 0.4 ± 0.2 % after 600 h aging at 50°C in the dark. Although the operational temperature of OPVs is usually below 65°C,[32-33] exposure to higher temperatures is possible during manufacturing, storage, transportation and installation. Additionally, stability tests at higher temperatures can accelerate the degradation channels. Therefore, we test the stability at temperatures up to 80°C. Figure 2 shows the PCE time evolution of the control (solid lines) and buffered (dashed lines) devices heated in the dark at several temperatures. At all temperatures, the addition of the C_{70} buffer improves the thermal stability. The T_{80} at 80°C improves from 20 min to 800 h with the addition of the C_{70} buffer. The control devices at 70°C and 80 °C show a recovery in their PCE after an initial decrease, forming a check-mark shaped aging pattern. The complete PCE time evolution up to 800 h can be found in SI (Fig. S2).

We apply the previously developed BQE analysis to understand which layers of the device are primarily responsible for the time-dependent changes in PCE.[27] The BQE measures the photogeneration properties of the BHJ that does not depend on the peripheral layers. The BQE is calculated using:

$$\mathrm{BQE}(V_{bulk}) = \frac{J_{ph}(V_{off} - V_{bulk})}{J_{sat}}, \quad (1)$$

where V_{bulk} is the voltage across the BHJ, J_{ph} is the photocurrent, V_{off} is the applied voltage at which J_{ph} is zero, and J_{sat} is the saturated photocurrent at a large reverse bias. In this work, J_{sat} is determined at a reverse bias of −2 V (see SI for the sensitivity of the results due to the choice of the reverse bias). Then, J_{ph}(V) can be obtained using:

$$J_{ph}(V) = J_{sat} \times BQE\left(V_{off} - V\right). \quad (2)$$

Here, V_{off} depends on the voltage drop across the layers *at* the periphery to the BHJ, or the device "edges".[31] In principle, J_{sat} depends on the recombination losses at the edges and is independent to the BQE, although this is not always the case (Fig. S6). Therefore, in following discussion, we use V_{off} only to characterize the effects of layers at the BHJ edges.

Figure 3(a) shows the time evolution of the BQE-V_{bulk} characteristics of the control device in the dark at 80 ºC. To better visualize the change of the BQE-V_{bulk} characteristics, the inset shows the time evolution of V_{80}, which is the V_{bulk} required to achieve a BQE of 80%, i.e. $V_{80} = V_{bulk}|_{\mathrm{BQE=80\%}}$.[27] It follows that charge extraction from the BHJ is more efficient for a smaller V_{80}. We observe that V_{80} increases rapidly in the first few hours, but recovers after 50 h. The BQE of the control devices at 60ºC and 70ºC shows a slower time evolution, but otherwise exhibits a similar behavior (Fig. S4). In contrast, Fig. 3(b) shows the time evolution of the BQE-V_{bulk} characteristics of a C_{70} buffered OPV at 80ºC, with V_{80} shown in the inset. The BQE and V_{80} remain almost unchanged after 600 h.

The time evolution of V_{off} of the control devices at several temperatures is shown in Fig. 3(c). The V_{off} shows a monotonic decrease of 0.12 ± 0.01 V(80ºC), 0.08 ± 0.01 V(70ºC), 0.07 ± 0.01 V(60ºC), 0.04 ± 0.01 V(50ºC) over 600 h. The time evolutions of V_{off} of C_{70} buffered devices at several temperatures are shown in Fig. 3(c). The V_{off} shows a smaller decrease of 0.07 ± 0.01 V(80ºC), 0.03 ± 0.01 V(70ºC), 0.02 ± 0.01 V(60ºC), 0.02 ± 0.01 V(50ºC) over 600 h. The monotonic decrease of V_{off} masks the BQE recovery of the control device at 60ºC, resulting in a less obvious recovery in the PCE at lower temperature.

From the foregoing, we identify two thermal degradation modes: (1) a temperature-induced change in the BHJ featured by the decrease and recovery of the BQE, which can be almost fully arrested by adding a thin C_{70} layer at the BHJ/MoO_x interface; and (2) an increased voltage loss at the BHJ periphery as inferred by the monotonic decrease of V_{off}. This voltage loss has been previously attributed to increased trapped charge that may form dipoles by attracting free charge at the opposite side of the interface between the BHJ and buffer layer.[16, 31]

To gain insights into the causes of mode (1), we examined the interfaces in devices with and without a C_{70} buffer via thin-section scanning transmission electron microscopy (STEM), and EDS. Figure 4(a) shows the bright-field (BF) STEM image of a control device heated in the dark for 700 h at 80 ºC, whereas Fig. 4(b) shows an image of the BHJ/MoO_x interface collected by a low-angle annular dark field (LAADF) detector. Figure 4(c) shows the Cl concentration (by weight) distributions of the as-cast and thermally aged devices with C_{70} buffer, and the thermally aged control device with the horizontal axis aligned to that of Fig. 4(a). Figure 4(d) shows the EDS Cl concentration map near the BHJ/MoO_x interface with the horizontal axis aligned to that of Fig. 4(b). An elevated Cl concentration is observed at the BHJ/MoO_x interface in the thermally aged control, but not in the as-cast and thermally aged C_{70} buffered devices. The Cl concentration can be distinguished in the LAADF (vertical bright line in the middle of Fig. 4(b) but not in the BF image. Among the materials comprising the device, only BT-CIC contains Cl. Therefore, we infer that the Cl concentration observed on the BHJ/MoO_x originates in the BHJ, which suggests a redistribution of Cl in the BHJ toward the BHJ/MoO_x interface during the thermal aging process. However, whether this redistribution is due to migration of Cl radicals, or the BT-CIC molecules, requires further study.

To understand the origin of the high Cl concentration at the BHJ/MoO_x interface in the thermally aged control, we used XPS to examine the MoO_x surface. Samples with structures: ITO (150 nm)/MoO_x (10 nm)/BT-CIC were prepared and thermally aged before submersion into chlorobenzene (CB) to dissolve the BT-CIC. Figures 5(a) and (b) show the XPS spectra of Mo 3d peaks of samples held at room temperature (RT) and 90°C, respectively. The spectra are fit with multiple Gaussian peaks using CasaXPS.[34] The intensity of Mo^{5+} relative to Mo^{6+} peak is reduced after the aging, suggesting that the MoO_x is oxidized. Figures 5(c) and (d) show the measured and fit XPS spectra of the Cl 2p peaks for samples held at RT and 90°C, respectively. The Cl peaks suggest the chlorination of MoO_x, possibly due to the smaller energy of the C-Cl bond (327 kJ/mol or 3.39 eV) compared that of Mo-Cl (365 kJ/mol or 3.78 eV).[35-36] Hence, this bond exchange is net exothermic. It should be noted that sulfur (S) 2s peak would appear if there are residual organic molecules on the MoO_x surface. Compared to the poor solubility of polymer donor, PCE-10 with observed S 2s peak at 228.3 eV (Fig. S7), the missing of S 2s peaks in Fig. 5(a) and (b) indicates the complete removal of BT-CIC by the CB treatment.

We obtain similar results for the PM6:Y6, a fluorine-rich NFA-based system, (Fig. S3). Considering the that both chlorine and fluorine are halogens, we speculate that these trends may be common to all halogen-rich NFA systems.

3. Discussion

Given these results, we can infer a likely mechanism leading to the thermal degradation of the control device. As shown in Fig. 6, due to the redox reaction between the BT-CIC and MoO_x observed by XPS, the BT-CIC molecules near the BHJ/MoO_x interface lose Cl to the MoO_x, causing an increase in interfacial voltage loss, which partially contributes to mode (2) degradation.

This drives a thermally activated redistribution of Cl toward the BHJ/MoO_x interface, leading to a decrease in BQE. When the Cl redistribution is complete, the BQE recovers, resulting in the check-mark shaped mode (1) degradation. The insertion of the C_{70} layer at the BHJ/MoO_x interface prevents interactions between BT-CIC and the MoO_x, thus eliminating mode (1) and reducing mode (2). However, mode (2) is not completely eliminated as shown in Fig. 3(d). Figure 6 also shows the photocatalytic reaction between BT-CIC and ZnO that leads to decomposition of BT-CIC.[26] An IC-SAM inserted between the BHJ and ZnO and external filtering of UV light can effectively suppress these mechanisms.

In Table 1, we summarize various photo- and thermal degradation mechanisms in inverted PCE10:BT-CIC based OPVs. Besides the thermal degradation mechanisms studied in this work, there are two main sources of photodegradation, the photocatalytic reaction between NFA-based BHJ and ZnO, and UV induced BHJ damage. The former causes decomposition of BT-CIC, leading to a degradation to both the BHJ and the edges. This reaction can be suppressed by inserting an IC-SAM or C_{60}-SAM between the BHJ and ZnO. The latter mainly affects the BHJ and can be suppressed by adding a cost-efficient UV-absorbing ZnO layer on the distal surface of the device.[26] With all the suppressing methods applied, the device has only an intrinsic photodegradation affecting the BHJ and a reduced mode (2) photodegradation affecting the edges (Fig. S5). Although the mechanisms in Table 1 may be specific to the materials and device structures in this study, the experimental and analytical methodologies introduced are general for separating extrinsic from intrinsic degradation mechanisms.

4. Conclusion

In summary, we identify and quantitatively study two different thermal degradation modes in inverted halogen-rich NFA-based OPVs with MoO_x as the HTL. Mode (1) results in a rapid 40% decrease of PCE followed by a slower recovery, forming a check-mark shaped aging pattern. The first mode affects the BHJ and is possibly due to a redox reaction between BHJ and MoO_x. A thin C_{70} layer inserted between the MoO_x and the BHJ effectively halts this degradation route. Mode (2) appears as a monotonically increasing voltage loss in the edges but does not affect the BHJ, and can only be partially suppressed by the additional C_{70} layer. The T_{80} increases from 20 min to 800 h with the insertion of the C_{70} buffer. The work provides results that move us closer to identification, and a more complete understanding of OPV failure mechanisms. Importantly, this work provides a general method by which these objectives can be met.

5. Experimental Methods

Device Fabrication, Thermal Aging and J-V Measurement. All devices were fabricated on ITO coated glass substrates (Lumtec Corp.) with a sheet resistance of 15 Ω/sq. The ITO anodes were patterned into 1 mm wide strips. The substrates were cleaned using a detergent (tergitol solution) and solvents (acetone and isopropanol) and exposed to ultraviolet-ozone for 15 min. The ZnO layer was deposited by spinning a sol-gel ZnO precursor solution (Sigma-Aldrich Inc.) at 4000 rpm for 1 min and thermally annealed in air at 160 ºC for 30 min. The IC-SAM was dissolved at 1 mg/mL in methanol and stirred at 300 rpm at 65 ºC overnight. The solution was then spun at 3500 rpm for 1 min, followed by thermally annealing at 110 ºC for 10 min. After the annealing, pure methanol solution was spun on the IC-SAM at 3500 rpm for 1 min to remove residual molecules that are not chemically bonded to the ZnO. The PCE-10:BT-CIC powder (99+%, 1-

Material Inc.) was dissolved in 9:1 chlorobenzene:chloroform solution at a total concentration of 16 mg/mL and stirred at 300 rpm at 65 °C overnight. The solution was then spun onto the sample at 4000 rpm for 1 min. The MoO_x layers and Ag electrodes were deposited in a vacuum thermal evaporation (VTE) chamber with a base pressure of 10^{-7} Torr. The MoO_x (99.9995%, Alfa Aesar) was deposited at 0.6 Å/s. The Ag was deposited at a rate ramped from 0.1 to 1 Å/s. The deposition rates and film thicknesses were monitored by quartz crystal monitors and calibrated post-growth using variable-angle spectroscopic ellipsometry. The Ag electrodes were deposited through 2 mm wide shadow mask openings oriented orthogonal to the ITO strips, forming device areas of 2 mm^2. After the deposition of the electrodes, the devices were encapsulated in N_2 atmosphere by cementing a top glass cover to the substrate with an epoxy (EPO-TEK® OG159-2, Epoxy Technology) bead around its periphery and UV cured for 100 s. The epoxy is not in direct contact with the device area.

The encapsulated devices were thermally aged on hotplates at various temperatures in air in the dark. The *J-V* characteristics were measured inside a N_2 glovebox at room temperature using a parameter analyzer (Agilent 4156C) with a 1 kW m^{-2} simulated AM 1.5G illumination source.

STEM, EDS and XPS Measurement. Cross-sectional slices of the OPVs were obtained via focused ion beam (FIB) milling (FEI Nova 200 Nanolab SEM/FIB) and glued by Pt soldering onto a lift-out grid rod. The sample is then thinned before transfer into the STEM (Thermo Fisher Talos F200X G2 S/TEM). The EDS integration time for each sample is 40 min.

Samples for XPS measurement have structures: ITO (150 nm)/MoO_x (10 nm)/organic layer were prepared on unpatterned ITO coated glass substrates using the same processes as for the OPVs. The organic layer is either a neat BT-CIC layer, or a PCE-10: BT-CIC, 1:2, blended layer. The samples are held at either RT or 90°C for 100 h before submersion into chlorobenzene to

dissolve the organic layer. All procedures are performed on samples in a N_2 filled glovebox, and then transferred into an ultra-high vacuum chamber (base pressure ~1 x 10^{-9} Torr) to perform XPS measurements (Kratos Axis Ultra XPS). The integration time for each spectrum is 25 min.

Acknowledgements

We thank Xiaheng Huang and Xinjing Huang for helpful discussions. This work was funded by the U.S. Department of the Navy, Office of Naval Research under Award No. N00014-17-1-2211, Universal Display Corporation and the U.S. Department of Energy's Office of Energy Efficiency and Renewable Energy (EERE) under Solar Energy Technologies Office (SETO) Agreement Number DE-EE0008561. This report was prepared as an account of work sponsored by an agency of the United States Government. Neither the United States Government nor any agency thereof, nor any of their employees, makes any warranty, express or implied, or assumes any legal liability or responsibility for the accuracy, completeness, or usefulness of any information, apparatus, product, or process disclosed, or represents that its use would not infringe privately owned rights. Reference herein to any specific commercial product, process, or service by trade name, trademark, manufacturer, or otherwise does not necessarily constitute or imply its endorsement, recommendation, or favoring by the United States Government or any agency thereof. The views and opinions of authors expressed herein do not necessarily state or reflect those of the United States Government or any agency thereof. This work also received technical support from the Michigan Center for Materials Characterization (Dr. Tao Ma and Dr. Haiping Sun).

Conflict of Interest

One of the authors of this work (S. R. F.) has an equity interest in one of the sponsors (Universal Display Corp.). This conflict is under management by the University of Michigan Office of Research.

References

1. Liu, Q.; Jiang, Y.; Jin, K.; Qin, J.; Xu, J.; Li, W.; Xiong, J.; Liu, J.; Xiao, Z.; Sun, K.; Yang, S.; Zhang, X.; Ding, L., 18% Efficiency Organic Solar Cells. *Sci. Bull.* **2020,** *65* (4), 272-275.

2. Riede, M.; Spoltore, D.; Leo, K., Organic Solar Cells—the Path to Commercial Success. *Adv. Energy Mater.* **2021,** *11* (1), 2002653.

3. Karki, A.; Gillett, A. J.; Friend, R. H.; Nguyen, T.-Q., The Path to 20% Power Conversion Efficiencies in Nonfullerene Acceptor Organic Solar Cells. *Adv. Energy Mater.* **2021,** *11* (15), 2003441.

4. Zhang, M.; Zhu, L.; Zhou, G.; Hao, T.; Qiu, C.; Zhao, Z.; Hu, Q.; Larson, B. W.; Zhu, H.; Ma, Z.; Tang, Z.; Feng, W.; Zhang, Y.; Russell, T. P.; Liu, F., Single-Layered Organic Photovoltaics with Double Cascading Charge Transport Pathways: 18% Efficiencies. *Nat. Commun.* **2021,** *12* (1), 309.

5. Duan, L.; Uddin, A., Progress in Stability of Organic Solar Cells. *Adv. Sci.* **2020,** *7* (11), 1903259.

6. Duan, L.; Yi, H.; Zhang, Y.; Haque, F.; Xu, C.; Uddin, A., Comparative Study of Light- and Thermal-Induced Degradation for Both Fullerene and Non-Fullerene-Based Organic Solar Cells. *Sustain. Energy Fuels* **2019,** *3* (3), 723-735.

7. Oh, S.; Song, C. E.; Lee, T.; Cho, A.; Lee, H. K.; Lee, J.-C.; Moon, S.-J.; Lim, E.; Lee, S. K.; Shin, W. S., Enhanced Efficiency and Stability of Ptb7-Th-Based Multi-Non-Fullerene Solar Cells Enabled by the Working Mechanism of the Coexisting Alloy-Like Structure and Energy Transfer Model. *J. Mater. Chem. A* **2019,** *7* (38), 22044-22053.

8. Duan, L.; Guli, M.; Zhang, Y.; Yi, H.; Haque, F.; Uddin, A., The Air Effect in the Burn-in Thermal Degradation of Nonfullerene Organic Solar Cells. *Energy Technol.* **2020,** *8* (5), 1901401.

9. Cha, H.; Wu, J.; Wadsworth, A.; Nagitta, J.; Limbu, S.; Pont, S.; Li, Z.; Searle, J.; Wyatt, M. F.; Baran, D.; Kim, J.-S.; McCulloch, I.; Durrant, J. R., An Efficient, "Burn in" Free Organic Solar Cell Employing a Nonfullerene Electron Acceptor. *Adv. Mater.* **2017,** *29* (33), 1701156.

10. Ye, L.; Gao, M.; Hou, J., Advances and Prospective in Thermally Stable Nonfullerene Polymer Solar Cells. *Sci. China Chem.* **2021**.

11. Sachs-Quintana, I. T.; Heumüller, T.; Mateker, W. R.; Orozco, D. E.; Cheacharoen, R.; Sweetnam, S.; Brabec, C. J.; McGehee, M. D., Electron Barrier Formation at the Organic-Back Contact Interface Is the First Step in Thermal Degradation of Polymer Solar Cells. *Adv. Func. Mater.* **2014,** *24* (25), 3978-3985.

12. Campoy-Quiles, M.; Ferenczi, T.; Agostinelli, T.; Etchegoin, P. G.; Kim, Y.; Anthopoulos, T. D.; Stavrinou, P. N.; Bradley, D. D. C.; Nelson, J., Morphology Evolution Via Self-Organization and Lateral and Vertical Diffusion in Polymer:Fullerene Solar Cell Blends. *Nat. Mater.* **2008,** *7* (2), 158-164.

13. Xu, Z.; Chen, L.-M.; Yang, G.; Huang, C.-H.; Hou, J.; Wu, Y.; Li, G.; Hsu, C.-S.; Yang, Y., Vertical Phase Separation in Poly(3-Hexylthiophene): Fullerene Derivative Blends and Its Advantage for Inverted Structure Solar Cells. *Adv. Func. Mater.* **2009,** *19* (8), 1227-1234.

14. Hermerschmidt, F.; Savva, A.; Georgiou, E.; Tuladhar, S. M.; Durrant, J. R.; McCulloch, I.; Bradley, D. D. C.; Brabec, C. J.; Nelson, J.; Choulis, S. A., Influence of the Hole Transporting Layer on the Thermal Stability of Inverted Organic Photovoltaics Using Accelerated-Heat Lifetime Protocols. *ACS Appl. Mater. Interfaces* **2017,** *9* (16), 14136-14144.

15. Greenbank, W.; Rolston, N.; Destouesse, E.; Wantz, G.; Hirsch, L.; Dauskardt, R.; Chambon, S., Improved Mechanical Adhesion and Electronic Stability of Organic Solar Cells with

Thermal Ageing: The Role of Diffusion at the Hole Extraction Interface. *J. Mater. Chem. A* **2017,** *5* (6), 2911-2919.

16. Yin, Y.; Pan, X.; Andersson, M. R.; Lewis, D. A.; Andersson, G. G., Mechanism of Organic Solar Cell Performance Degradation Upon Thermal Annealing of Moox. *ACS Appl. Energy Mater.* **2020,** *3* (1), 366-376.

17. Son, H. J.; Park, H.-K.; Moon, J. Y.; Ju, B.-K.; Kim, S. H., Thermal Degradation Related to the Pedot:Pss Hole Transport Layer and Back Electrode of the Flexible Inverted Organic Photovoltaic Module. *Sustain. Energy Fuels* **2020,** *4* (4), 1974-1983.

18. Ghosekar, I. C.; Patil, G. C., Performance Analysis and Thermal Reliability Study of Multilayer Organic Solar Cells. *IEEE Trans. Device Mater. Reliab.* **2019,** *19* (3), 572-580.

19. Albonetti, C.; El Qacemi, V.; Limage, S.; Versini, C.; Kauffmann, L.-D.; Muccini, M.; Seri, M., Enhanced Thermal Stability of Inverted Polymer Solar Cells Based on Solution-Processed Wox as an Anode Interlayer. *Phys. Status Solidi A* **2021,** *218* (8), 2000748.

20. Kim, J.; Lee, Y.; Kim, J. Y.; Song, H.-J.; Song, J.; Lee, H.; Lee, C., Analysis of the Improved Thermal Stability of Al-Doped Zno-Adopted Organic Solar Cells. *Appl. Phys. Lett.* **2021,** *118* (2), 023302.

21. Voroshazi, E.; Uytterhoeven, G.; Cnops, K.; Conard, T.; Favia, P.; Bender, H.; Muller, R.; Cheyns, D., Root-Cause Failure Analysis of Photocurrent Loss in Polythiophene:Fullerene-Based Inverted Solar Cells. *ACS Appl. Mater. Interfaces* **2015,** *7* (1), 618-623.

22. Rösch, R.; Tanenbaum, D. M.; Jørgensen, M.; Seeland, M.; Bärenklau, M.; Hermenau, M.; Voroshazi, E.; Lloyd, M. T.; Galagan, Y.; Zimmermann, B.; Würfel, U.; Hösel, M.; Dam, H. F.; Gevorgyan, S. A.; Kudret, S.; Maes, W.; Lutsen, L.; Vanderzande, D.; Andriessen, R.; Teran-Escobar, G.; Lira-Cantu, M.; Rivaton, A.; Uzunoğlu, G. Y.; Germack, D.; Andreasen, B.; Madsen,

M. V.; Norrman, K.; Hoppe, H.; Krebs, F. C., Investigation of the Degradation Mechanisms of a Variety of Organic Photovoltaic Devices by Combination of Imaging Techniques—the Isos-3 Inter-Laboratory Collaboration. *Energy Environ. Sci.* **2012,** *5* (4), 6521-6540.

23. Lloyd, M. T.; Olson, D. C.; Lu, P.; Fang, E.; Moore, D. L.; White, M. S.; Reese, M. O.; Ginley, D. S.; Hsu, J. W. P., Impact of Contact Evolution on the Shelf Life of Organic Solar Cells. *J. Mater. Chem.* **2009,** *19* (41), 7638-7642.

24. Sung, Y.; Huang, Y.; Chien, F. S.; Tsao, C., Mechanism and Analysis of Thermal Burn-in Degradation of Opvs Induced by Evaporated Htl. *IEEE J. Photovolt.* **2019,** *9* (3), 694-699.

25. Schloemer, T. H.; Raiford, J. A.; Gehan, T. S.; Moot, T.; Nanayakkara, S.; Harvey, S. P.; Bramante, R. C.; Dunfield, S.; Louks, A. E.; Maughan, A. E.; Bliss, L.; McGehee, M. D.; van Hest, M. F. A. M.; Reese, M. O.; Bent, S. F.; Berry, J. J.; Luther, J. M.; Sellinger, A., The Molybdenum Oxide Interface Limits the High-Temperature Operational Stability of Unencapsulated Perovskite Solar Cells. *ACS Energy Lett.* **2020,** *5* (7), 2349-2360.

26. Li, Y.; Huang, X.; Ding, K.; Sheriff, H. K. M.; Ye, L.; Liu, H.; Li, C.-Z.; Ade, H.; Forrest, S. R., Non-Fullerene Acceptor Organic Photovoltaics with Intrinsic Operational Lifetimes over 30 Years. *Nat. Commun.* **2021,** *12* (1), 5419.

27. Ding, K.; Huang, X.; Li, Y.; Forrest, S. R., Photogeneration and the Bulk Quantum Efficiency of Organic Photovoltaics. *Energy Environ. Sci.* **2021,** *14* (3), 1584-1593.

28. Li, Y.; Guo, X.; Peng, Z.; Qu, B.; Yan, H.; Ade, H.; Zhang, M.; Forrest, S. R., Color-Neutral, Semitransparent Organic Photovoltaics for Power Window Applications. *Proc. Natl. Acad. Sci.* **2020,** *117* (35), 21147-21154.

29. Huang, X.; Sun, B.; Li, Y.; Jiang, C.; Fan, D.; Fan, J.; Forrest, S. R., 15.9% Organic Tandem Solar Cell with Extended near-Infrared Absorption. *Appl. Phys. Lett.* **2020,** *116* (15), 153501.

30. Li, Y.; Lin, J.-D.; Liu, X.; Qu, Y.; Wu, F.-P.; Liu, F.; Jiang, Z.-Q.; Forrest, S. R., Near-Infrared Ternary Tandem Solar Cells. *Adv. Mater.* **2018,** *30* (45), 1804416.

31. Ding, K.; Forrest, S. R., Reducing Energy Losses at the Organic--Anode-Buffer Interface of Organic Photovoltaics. *Phys. Rev. Appl.* **2020,** *13* (5), 054046.

32. Burlingame, Q.; Zanotti, G.; Ciammaruchi, L.; Katz, E. A.; Forrest, S. R., Outdoor Operation of Small-Molecule Organic Photovoltaics. *Org. Electron.* **2017,** *41*, 274-279.

33. Zhang, Y.; Samuel, I. D. W.; Wang, T.; Lidzey, D. G., Current Status of Outdoor Lifetime Testing of Organic Photovoltaics. *Adv. Sci.* **2018,** *5* (8), 1800434.

34. Fairley, N.; Fernandez, V.; Richard-Plouet, M.; Guillot-Deudon, C.; Walton, J.; Smith, E.; Flahaut, D.; Greiner, M.; Biesinger, M.; Tougaard, S.; Morgan, D.; Baltrusaitis, J., Systematic and Collaborative Approach to Problem Solving Using X-Ray Photoelectron Spectroscopy. *Appl. Surf. Sci. Adv.* **2021,** *5*, 100112.

35. Benson, S. W., III - Bond Energies. *J. Chem. Educ.* **1965,** *42* (9), 502.

36. Haynes, W. M., *Crc Handbook of Chemistry and Physics*. CRC Press: 2014.

37. Park, S.; Son, H. J., Intrinsic Photo-Degradation and Mechanism of Polymer Solar Cells: The Crucial Role of Non-Fullerene Acceptors. *J. Mater. Chem. A* **2019,** *7* (45), 25830-25837.

38. Jiang, Y.; Sun, L.; Jiang, F.; Xie, C.; Hu, L.; Dong, X.; Qin, F.; Liu, T.; Hu, L.; Jiang, X.; Zhou, Y., Photocatalytic Effect of Zno on the Stability of Nonfullerene Acceptors and Its Mitigation by Sno2 for Nonfullerene Organic Solar Cells. *Mater. Horiz.* **2019,** *6* (7), 1438-1443.

39. Rivaton, A.; Tournebize, A.; Gaume, J.; Bussière, P.-O.; Gardette, J.-L.; Therias, S., Photostability of Organic Materials Used in Polymer Solar Cells. *Polym. Int.* **2014,** *63* (8), 1335-1345.

40. Classen, A.; Heumueller, T.; Wabra, I.; Gerner, J.; He, Y.; Einsiedler, L.; Li, N.; Matt, G. J.; Osvet, A.; Du, X.; Hirsch, A.; Brabec, C. J., Revealing Hidden Uv Instabilities in Organic Solar Cells by Correlating Device and Material Stability. *Adv. Energy Mater.* **2019,** *9* (39), 1902124.

41. White, R. T.; Thibau, E. S.; Lu, Z.-H., Interface Structure of Moo3 on Organic Semiconductors. *Sci. Rep.* **2016,** *6*, 21109.

42. Yan, L.; Gu, H.; Li, Z.; Zhang, J.; Yang, Y.; Wang, H.; Liu, X.; Wei, Z.; Luo, Q.; Ma, C.-Q., The Interfacial Degradation Mechanism of Polymer:Fullerene Bis-Adduct Solar Cells and Their Stability Improvement. *Mater. Adv.* **2020,** *1* (5), 1307-1317.

43. Xie, F.; Choy, W. C. H.; Wang, C.; Li, X.; Zhang, S.; Hou, J., Low-Temperature Solution-Processed Hydrogen Molybdenum and Vanadium Bronzes for an Efficient Hole-Transport Layer in Organic Electronics. *Adv. Mater.* **2013,** *25* (14), 2051-2055.

Tables

Table 1. Effects of various photo- and thermal degradation mechanisms in PCE-10:BT-CIC inverted OPVs and methods to suppress them.

Mechanism	Type	Effects	Method to Suppress
Photocatalytic reaction between BHJ and ZnO [37-38]	Photo-	Decrease of BQE and V_{off}	Inserting an IC-SAM or C_{60}-SAM between the BHJ and ZnO [26-27]
UV exposure [39-40]	Photo-	Decrease of BQE	Adding a UV-absorbing ZnO coating on the distal surface of the device [26]
Intrinsic photodegradation of the BHJ under white light	Photo-	Decrease of BQE	
Mode (1) thermal degradation of the BHJ	Thermal	Check-mark shaped aging pattern of BQE	Inserting a 2-nm-thick C_{70} buffer between the BHJ and MoO_x
Mode (2) thermal degradation of the edges [41-43]	Thermal	Decrease of V_{off}	Partially suppressed by the C_{70} buffer

Figure Captions

Figure 1. (a) Time evolution of the current density voltage (*J-V*) characteristics of a PCE-10:BT-CIC device when heated at 50°C in the dark. Inset: Device structure. (b) Time evolution of *J-V* characteristics of a PCE-10:BT-CIC device with a 2 nm thick C_{70} layer inserted between the MoO_x and BHJ when heated at 50°C in the dark. Inset: Device structure.

Figure 2. Time evolution of power conversion efficiencies (PCEs) of control devices (solid lines) and devices with the C_{70} protection layer (dashed lines) aged at various temperatures. The errors of the PCEs are ± 0.2 %.

Figure 3. (a) Time evolution of the bulk quantum efficiency (BQE) vs. the voltage on the BHJ (V_{bulk}) characteristics of a control device aged at 80°C. Inset: Time evolution of V_{bulk} to reach a BQE of 80% (V_{80}). (b) Time evolution of BQE-V_{bulk} characteristics of a C_{70} buffered device aged at 80°C. Inset: time evolution of V_{80}. (c) Time evolution of V_{off} of control devices aged at various temperatures. (d) Time evolution of V_{off} of C_{70} buffered devices aged at various temperatures.

Figure 4. (a) Scanning transmission electron microscope (STEM) image collected by a bright-field (BF) detector of a control device aged in the dark for 700 h at 80°C. (b) Magnified STEM image of the BHJ/MoO_x interface collected by a low-angle annular dark field (LAADF) detector. (c) The Cl weight concentration distributions of the as-cast device with a C_{70} layer, the thermally aged device with a C_{70} layer and the thermally aged control device with the horizontal axis aligned to that in (a). (d) The Cl weight concentration map near the BHJ/MoO_x interface in the thermally aged control device with the horizontal axis aligned to that in (b).

Figure 5. X-ray photoelectron spectra (XPS) of the Mo 3d signal of MoO_x layers fabricated with BT-CIC layers held at (a) room temperature (RT) and (b) 90°C for 100 h. XPS spectra of Cl 2p of MoO_x layers fabricated with BT-CIC layers held at (c) RT and (d) 90°C for 100 h.

Figure 6. Left: Proposed photo- and thermal degradation mechanisms in PCE-10:BT-CIC inverted OPVs. Right: Modified structure that effectively suppresses the degradation mechanisms illustrated at left.

For Table of Contents Only

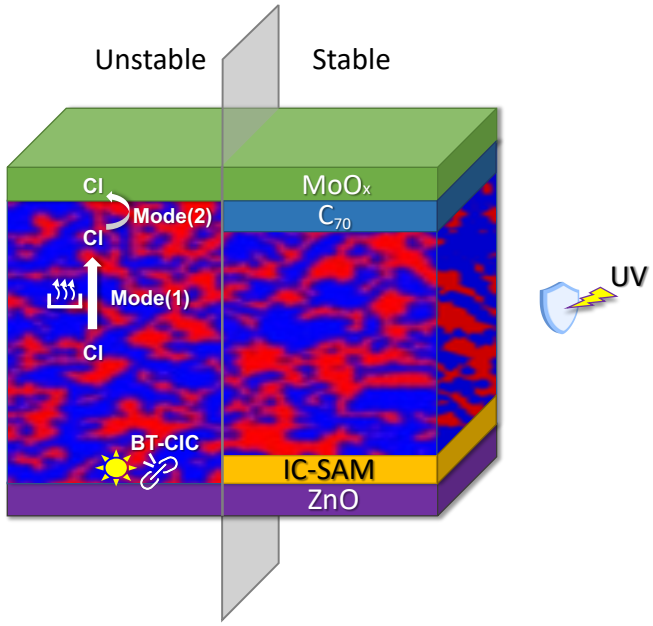

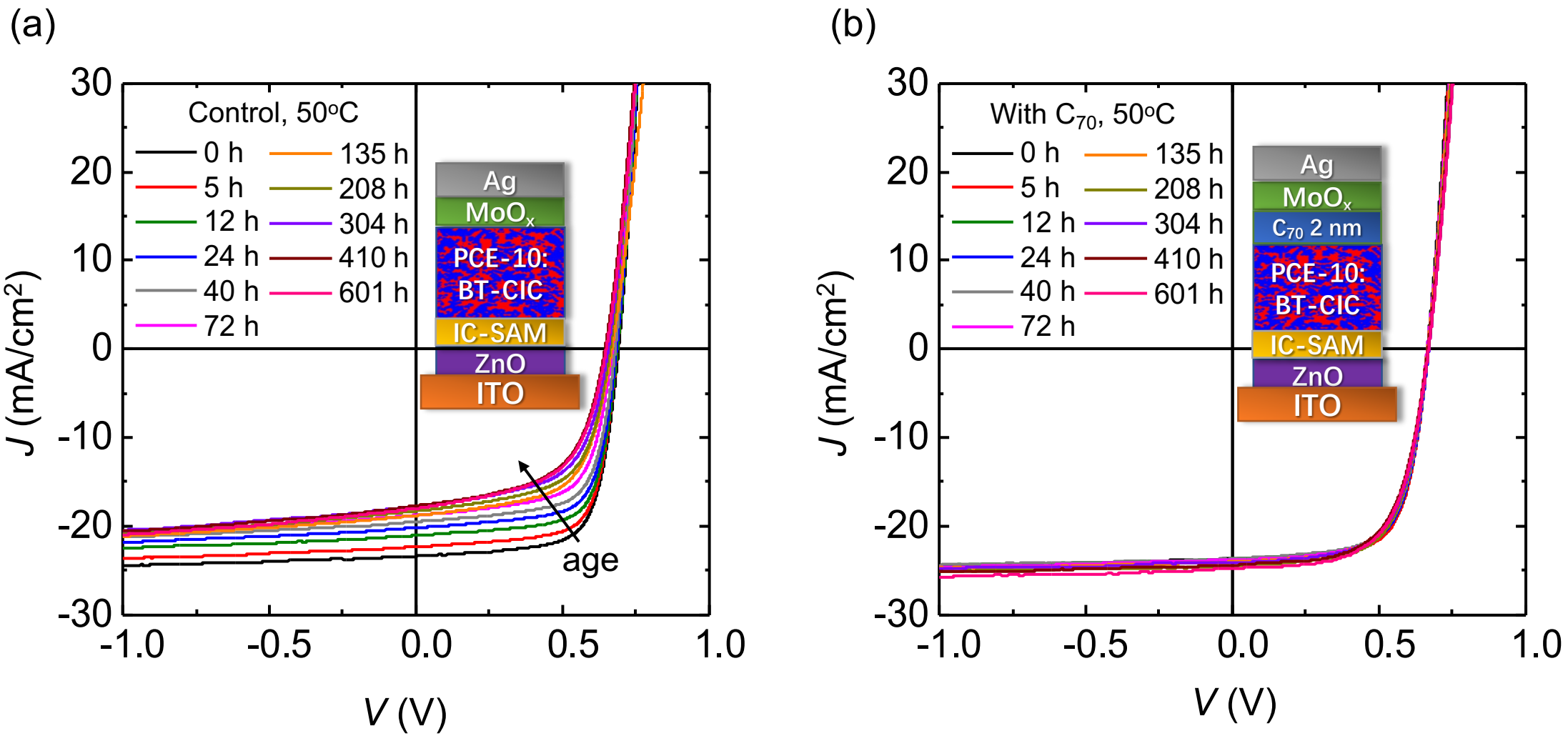
(a)
Control, 50°C
0 h
5 h
12 h
24 h
40 h
72 h
135 h
208 h
304 h
410 h
601 h
Ag
MoOx
PCE-10:
BT-CIC
IC-SAM
ZnO
ITO
age
J (mA/cm²)
V (V)
(b)
With C70, 50°C
C70 2 nm

Figure 1

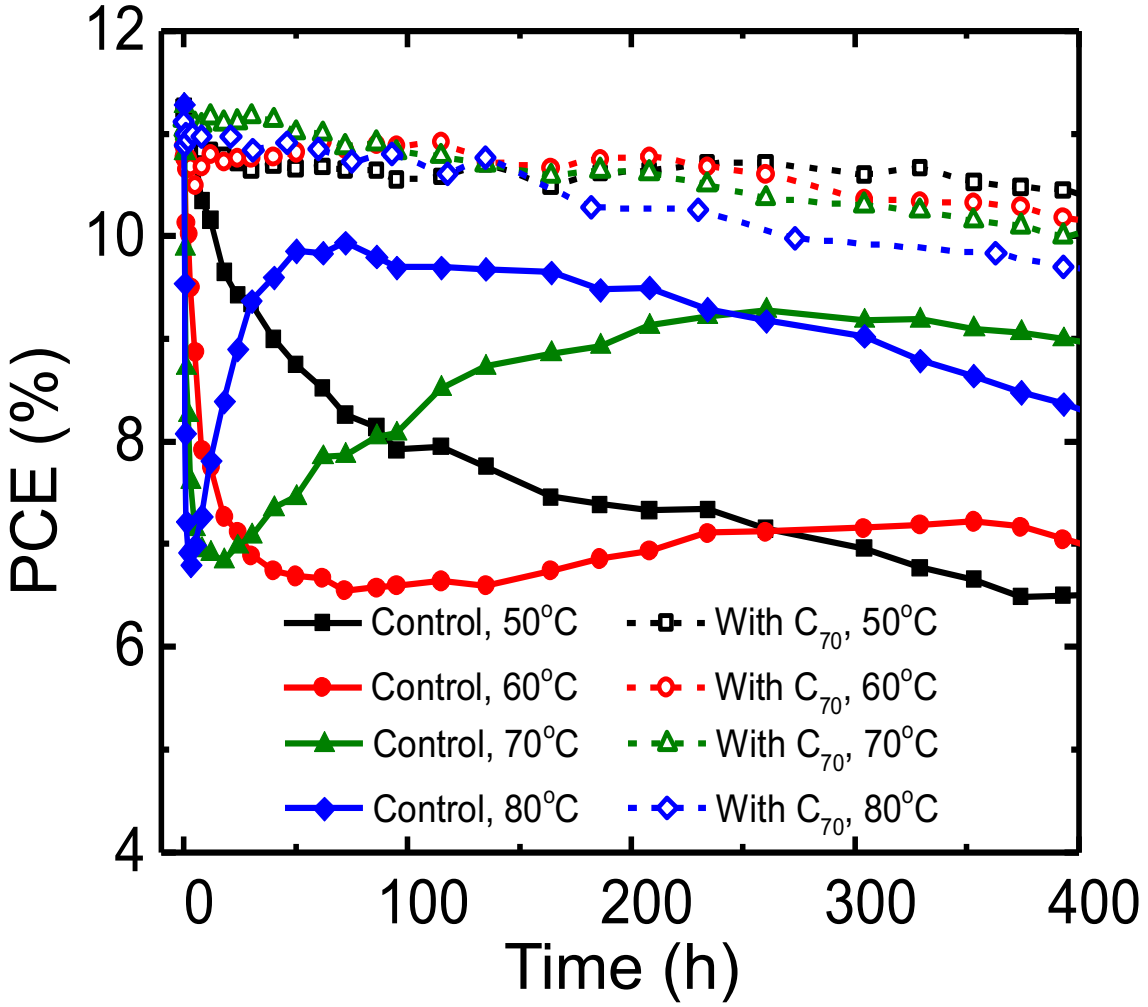
12
10
8
6
4
PCE (%)
0
100
200
300
400
Time (h)
Control, 50°C
With C70, 50°C
Control, 60°C
With C70, 60°C
Control, 70°C
With C70, 70°C
Control, 80°C
With C70, 80°C

Figure 2

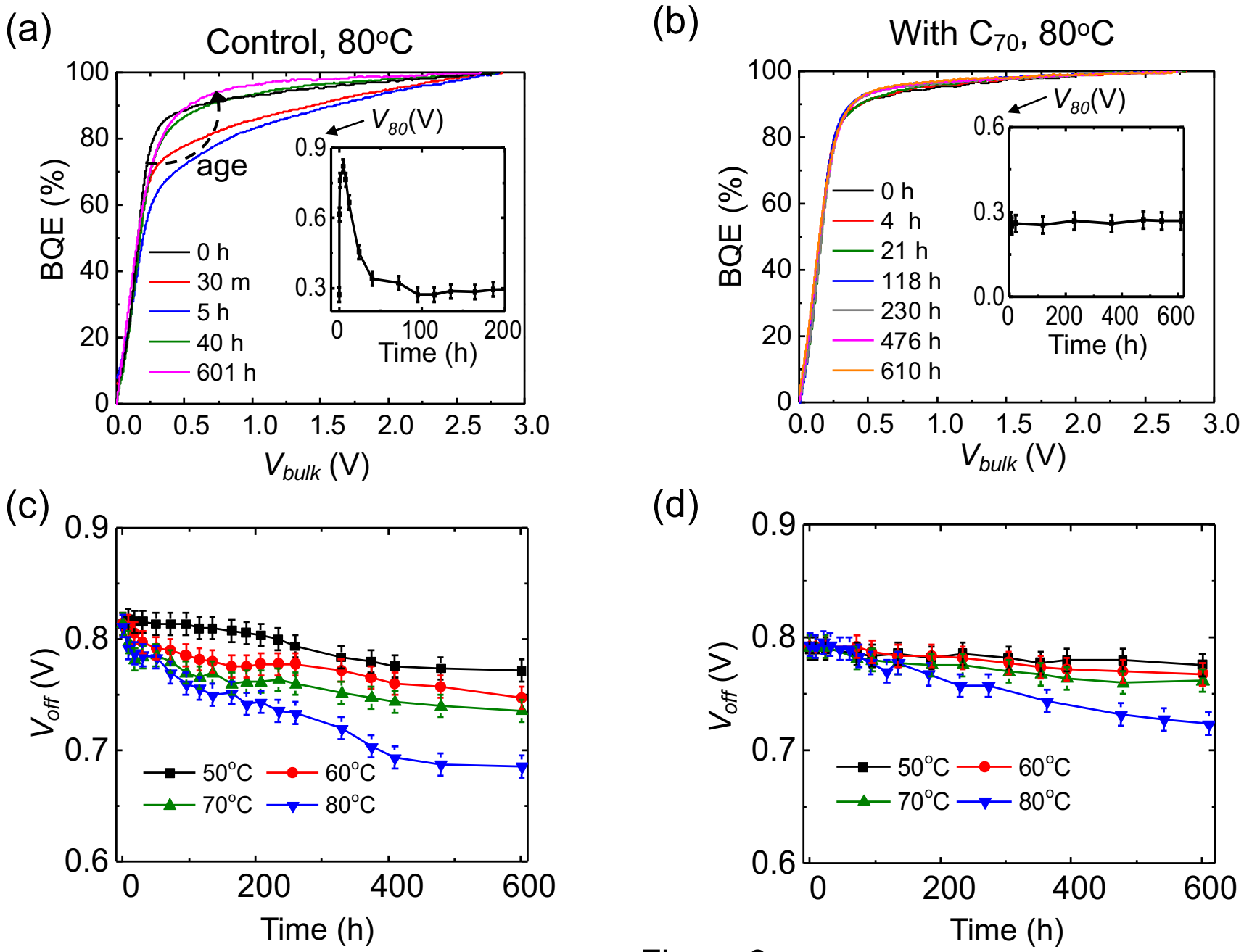
(a)
Control, 80°C
BQE (%)
V_{bulk} (V)
age
0 h
30 m
5 h
40 h
601 h
V_{80}(V)
Time (h)
(b)
With C_{70}, 80°C
BQE (%)
V_{bulk} (V)
0 h
4 h
21 h
118 h
230 h
476 h
610 h
V_{80}(V)
Time (h)
(c)
V_{off} (V)
50°C
60°C
70°C
80°C
Time (h)
(d)
V_{off} (V)
50°C
60°C
70°C
80°C
Time (h)

Figure 3

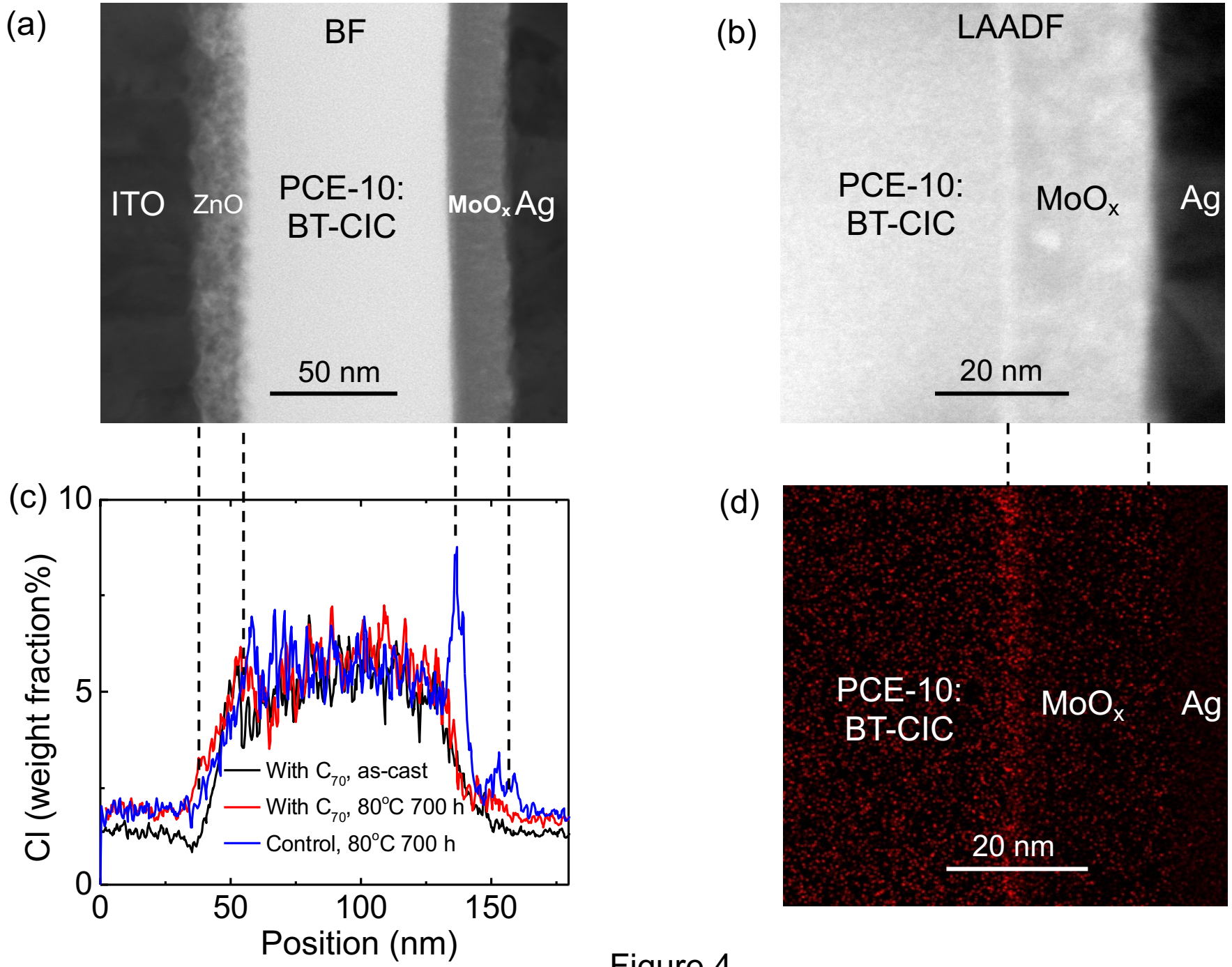
(a)
BF
ITO
ZnO
PCE-10:
BT-CIC
MoOx
Ag
50 nm
(b)
LAADF
PCE-10:
BT-CIC
MoOx
Ag
20 nm
(c)
Cl (weight fraction%)
10
5
0
0
50
100
150
Position (nm)
With C70, as-cast
With C70, 80°C 700 h
Control, 80°C 700 h
(d)
PCE-10:
BT-CIC
MoOx
Ag
20 nm

Figure 4

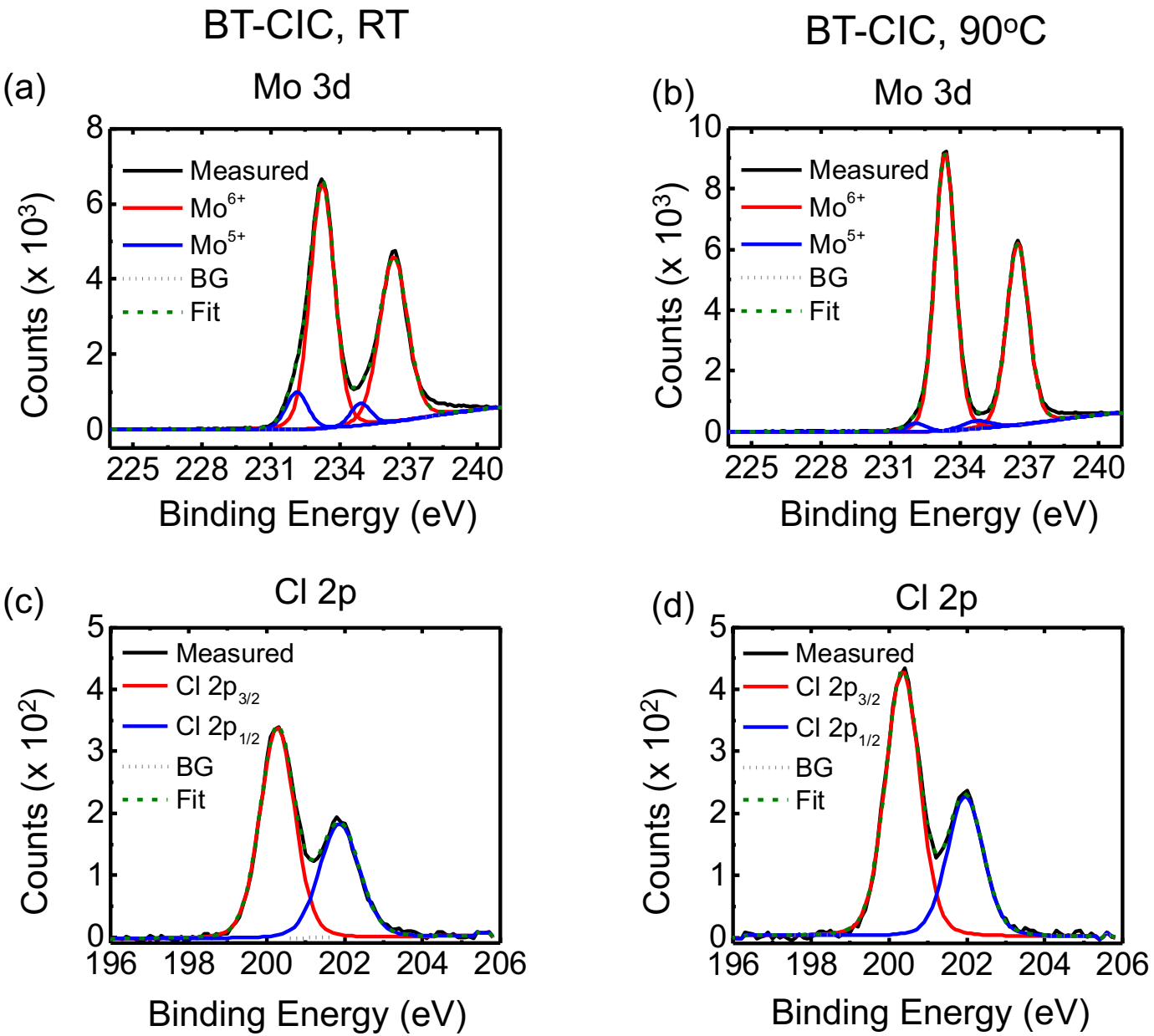
BT-CIC, RT
BT-CIC, 90°C
(a)
Mo 3d
(b)
Mo 3d
Counts (x 10³)
Measured
Mo⁶⁺
Mo⁵⁺
BG
Fit
Binding Energy (eV)
(c)
Cl 2p
(d)
Cl 2p
Counts (x 10²)
Cl 2p3/2
Cl 2p1/2

Figure 5

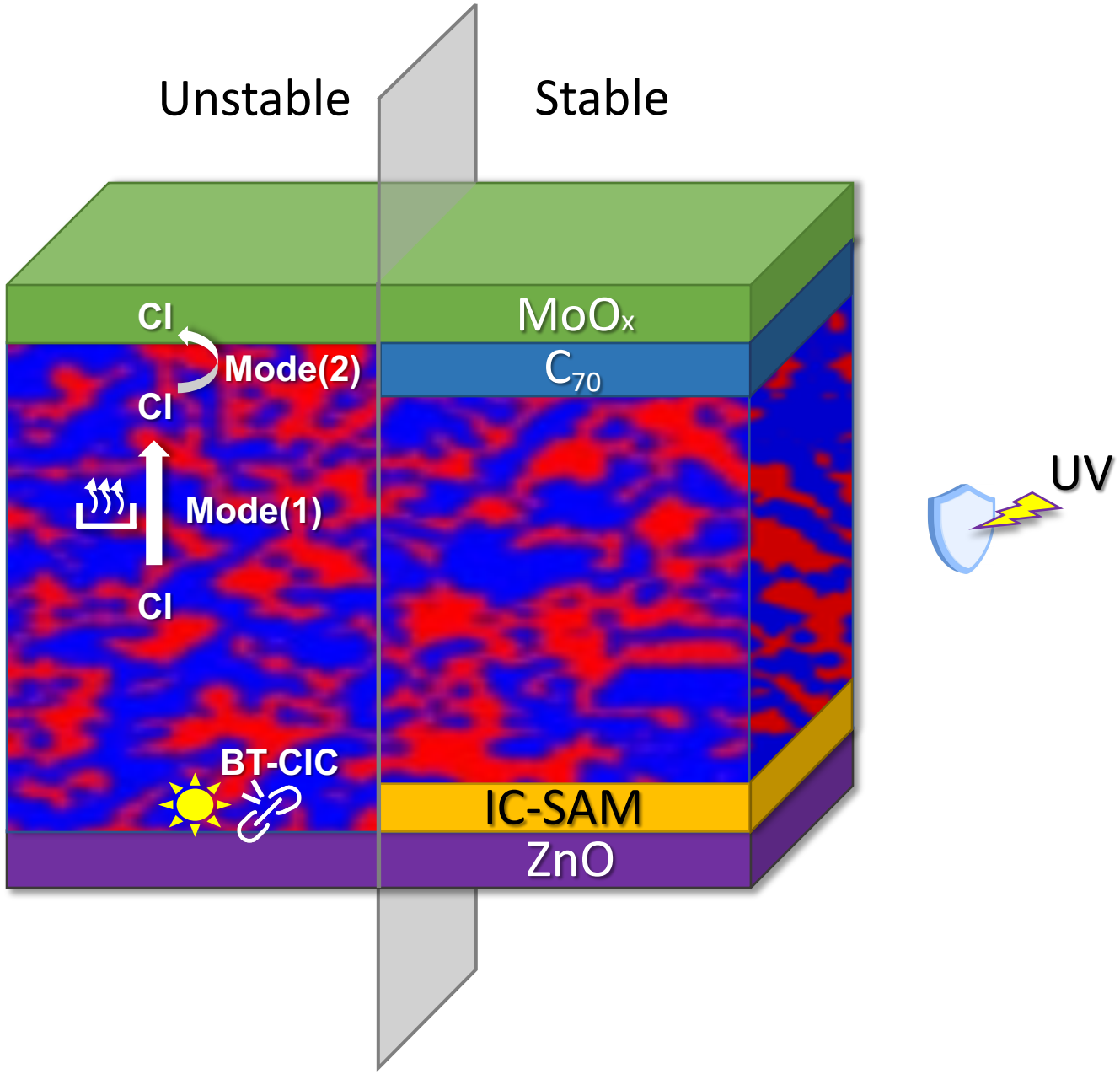
Unstable
Stable
Cl
Mode(2)
Cl
Mode(1)
Cl
BT-CIC
MoOx
C70
IC-SAM
ZnO
UV

Figure 6